

Revisiting Deep Architectures for Head Motion Prediction in 360° Videos

Miguel Fabián Romero Rondón, Lucile Sassatelli, Ramón Aparicio Pardo, Frédéric Precioso

Abstract—Head motion prediction is an important problem with 360° videos, in particular to inform the streaming decisions. Various methods tackling this problem with deep neural networks have been proposed recently. In this article we first show the startling result that all such existing methods, which attempt to benefit both from the history of past positions and knowledge of the video content, perform worse than a simple no-motion baseline. We then propose an LSTM-based architecture which processes the positional information only. It is able to establish state-of-the-art performance and we consider it our position-only baseline. Through a thorough root cause analysis, we first show that the content can indeed inform the head position prediction for horizons longer than 2 to 3s, the trajectory inertia being predominant earlier. We also identify that a sequence-to-sequence auto-regressive framework is crucial to improve the prediction accuracy over longer prediction windows, and that a dedicated recurrent network handling the time series of positions is necessary to reach the performance of the position-only baseline in the early prediction steps. This allows to make the most of the positional information and ground-truth saliency. Finally we show how the level of noise in the estimated saliency impacts the architecture’s performance, and we propose a new architecture establishing state-of-the-art performance with estimated saliency, supporting its assets with an ablation study.

I. INTRODUCTION

IMMERSIVE media are on the rise: Virtual Reality (VR) and augmented reality traffic is expected to increase 20-fold by 2021, while the market should reach \$215B in 2022 [1]. 360° videos are an important modality of VR, with applications in story-telling, journalism or remote education. Despite these exciting prospects, the development is persistently hindered by the difficulty to access immersive content through Internet streaming. Indeed, owing to the closer proximity of the screen to the eye in VR and to the width of the content (2π steradians in azimuth and π in elevation angles), the data rate is two orders of magnitude that of a regular video [2]. To decrease the amount of data to stream, a solution is to send in high resolution only the portion of the sphere the user has access to at each point in time, named the Field of View (FoV). To do so, recent works have proposed to either segment the video spatially into tiles and set the quality of the tiles according to their proximity to the FoV [3], [4], or use projections enabling high resolutions of regions close to the FoV [5]. These approaches however require to know the user’s head position in advance, that is at the time of sending the content from the server (see Fig. 1). Failing to predict correctly the future user’s positions can lead to a lower quality

displayed in the FoV, which can impair the user’s experience. When possible, the prediction error might be corrected when time progresses, by downloading again the same segments in higher quality to replace their low quality version close to the playout deadline. This however yields redundant transmissions and hence a higher consumed network rate. Let us mention that approaches based on Scalable Video Coding [6] may require prediction on shorter horizons, but the data overhead entailed by scalable coding represents an additional difficulty compared with regular Advanced Video Coding.

It is therefore crucial for an efficient 360° video streaming system to embed an accurate head motion predictor which can periodically inform, based on the past trajectory and on the content, where the user will be likely looking at over a future horizon. Various methods tackling this problem with deep neural networks have therefore been proposed in the last couple of years (e.g., [7], [8], [9], [10], [11]). In view of comparing them with each other (which none of them does), we obtain the startling result that all existing methods for this problem are outperformed by a trivial baseline. From this observation, we undertake a thorough root cause analysis of their weaknesses, which enables us to design new deep architectures that establish state-of-the-art performance and whose assets are supported with an ablation study.

Contributions:

- We propose a breakdown of the head motion prediction problem into subproblems for which we extract classes of choices made by the existing methods to tackle each of these subproblems. We thereby present a taxonomy and provide a structured and detailed review of the existing methods.
- We then compare each of the existing methods (PAMI18 [7], CVPR18 [8], MM18 [9], ChinaCom18 [10] and NOSSDAV17 [11]), on their original datasets, on their prediction horizons and using their metrics, with a trivial baseline assuming no motion. We obtain the striking result that all existing methods, without any exception, perform worse than this baseline. We then design a strong baseline aware of the past user’s positions only. The architecture is made of a single Long Short Term Memory (LSTM) layer embedded in a sequence-to-sequence auto-regressive framework. We show that this new proposal is able to outperform the no-motion baseline and hence establish state-of-the-art performance. This proposal is then coined *position-only* baseline, and becomes the benchmark for methods attempting at benefiting from both the video content and the positional information.
- We undertake a thorough analysis of the causes for the existing methods to perform worse than simple baselines. First, we analyze the choice of dataset and prediction horizon.

We introduce a so-called *saliency-only* baseline, to show that the relevance of the content information for the prediction depends on the video. Considering the content in the prediction can significantly help for non-Exploration videos if the prediction horizon is longer than 2 to 3s, but there is no guarantee it can significantly or easily help for shorter horizons, as done in all analyzed existing methods. Second, we analyze the choices of deep architectures to identify how to eventually benefit from the saliency-information. Considering the ground-truth saliency first (obtained from users' statistics) to remove any variability due to the choice of saliency extractor, we show that the sequence-to-sequence framework is crucial for efficient prediction and we propose improved versions of the representative methods CVPR18 and MM18. We show that the building block of CVPR18 is better fitted to the prediction problem, reaching the *position-only* baseline and approaching the *saliency-only* baseline over the entire prediction horizon.

- Considering finally a heat map estimated from the content with a saliency model, we uncover the impact of less accurate saliency information onto the improved CVPR18 architecture's performance, which substantially degrades away from the baselines again. We show that the reason is the inability of this architecture to handle the noise present in the estimated saliency. From this analysis we propose a new architecture which proves able to most benefit from both positional information and estimated saliency, thereby establishing state-of-the-art performance. We finally perform an ablation study to identify the essential components of this architecture.

Interest for the community: We believe our results can be most useful to the community, assessing the existing works against new common baselines, examining the possible causes for their weaknesses, and finally showing how to outperform these methods in all considered dataset and prediction horizon cases. They provide important guidelines on the type of method best suited to predict at lowest complexity depending on the problem settings.

Owing to the critical results and perspective we raise on the state-of-the-art, and in our concern for reproducibility, the entire code used to generate the results and plots will be made publicly available.

Sec. II formulates the exact prediction problem considered, and presents a taxonomy of the existing methods as well as a detailed description of each. Sec. III presents their comparison against two baselines, and provides important design elements of our position-only baseline. Sec. IV presents the first part of the root cause analysis by analyzing the video content and the user behavior. Sec. V is the second part of the root cause analysis, which investigates the architectural choices. Finally Sec. VI presents the impact of the approximated saliency on the architecture's performance, and how to overcome this difficulty by proposing a new architecture. Sec. VII concludes the article.

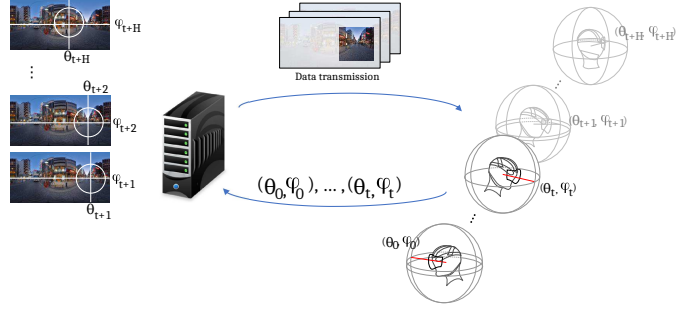


Fig. 1: **360° video streaming principle.** The user requests the next video segment at time t , if the future orientations of the user $(\theta_{t+1}, \varphi_{t+1}), \dots, (\theta_{t+H}, \varphi_{t+H})$ were known, the bandwidth consumption could be reduced by sending in higher quality only the areas corresponding to the future FoV.

II. REVIEW AND TAXONOMY OF EXISTING HEAD PREDICTION METHODS

This section reviews the existing methods relevant for the problem we consider. We hence start by formulating the exact problem which consists, at each video playback time t , in predicting the future user's head positions between t and $t + H$, as illustrated in Fig. 1 and represented in Fig. 2, with the only knowledge of this user's past positions and the (entire) video content. We therefore do not consider methods aiming at predicting the entire user trajectory from the start based on the content and the starting point as, e.g., targeted by a recent challenge [12] or summarizing a 360° video into 2D [13], [14]. Also, the domain of egocentric videos is related to that of 360° video. However, the assumptions are not exactly the same: only part of scene and some regions likely to attract the users are available (video shot from a mobile phone), contrary to a 360° video. We therefore do not compare with such works but recent architectures (such as in [15], [16]) are akin to some below (PAMI18 and CVPR18, respectively), and can be investigated in the same way. The problem we tackle is inherently dynamic and aims at helping streaming decisions made along the playback. We then present the existing methods and the classification we propose, based on the choices of deep neural network architecture. Finally, we provide a detailed description of each method we compare with in this article.

A. Problem formulation

Let $\mathbf{P}_t = [\theta_t, \varphi_t]$ denote the vector coordinates of the FoV at time t . Let \mathbf{V}_t denote the considered visual information at time t : depending on the tested models' assumptions, it can either be the raw frame with each RGB channel, or a 2D saliency map resulting from a pre-computed saliency extractor (embedding the motion information). Let H be the prediction horizon, as depicted in Fig. 2. We formulate the problem of trajectory prediction as finding the best model \mathbf{F}_H^* verifying:

$$\mathbf{F}_H^* = \arg \min \mathbb{E}_t \left[D \left([\mathbf{P}_{t+1}, \dots, \mathbf{P}_{t+H}], \mathbf{F}_H([\mathbf{P}_t, \dots, \mathbf{P}_0, \mathbf{V}_{t+H}, \mathbf{V}_{t+H-1}, \dots, \mathbf{V}_0]) \right) \right]$$

where $D(\cdot)$ is the chosen distance between the ground truth series of the future positions and the series of predicted positions. We define the terms *prediction step* and *time-stamp* as predicting for all prediction steps $s \in [0, H]$ from video time-stamp t . This depicted in Fig. 2. For every *time-stamp* $t \in [T_{start}, T]$ if T is the video duration, we run predictions $\hat{\mathbf{P}}_{t+s}$, for all *prediction steps* $s \in [0, H]$, where H denotes the *prediction horizon*. To stick to the settings of the works we compare with, T_{start} is set to $0s$ for all the curves generated in Sec. III. From Sec. IV, we set $T_{start} = 6s$ (to skip the exploration phase, as explained in Sec. IV-B). Then, for each s , we average the errors $dist(\hat{\mathbf{P}}_{t+s}, \mathbf{P}_{t+s})$ over all $t \in [T_{start}, T]$. We make H vary between $0.2s$ and $2.5s$, as considered in the existing methods we compare with, then beyond $2.5s$ as detailed from the analysis in Sec. IV.

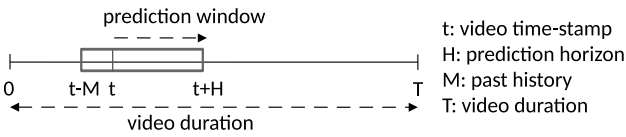


Fig. 2: For each time-stamp t , the next positions until $t + H$ are predicted.

B. Taxonomy

Various approaches to predict user motion in 360° video environments have been published lately, and are organized in Table I. First, for the sake of clarity, each considered method from the literature is named, as represented in column 1 (starting from the left), with the name of the conference or journal it was published in, appended with the year of publication. They consider different objectives (col. 2), such as predicting the future head position, gaze position or tiles in the FoV. The prediction horizons (col. 3) also span a wide range, from $30ms$ to $2.5s$. Some articles re-use the same datasets (col. 4), yet not comparing with these existing methods. Different types of input and input formats are considered (col. 5): some consider the positional information implicitly by only processing the content in the FoV, other consider the position separately, represented as a series of coordinates (e.g., CVPR18) or as a mask (e.g., MM18), with the last sample only (IC3D17) or various length of history, some extract features from the visual content by employing some pre-trained saliency extractors (e.g. NOSSDAV17, CVPR18) or training end-to-end representation layers made of convolutional and maxpooling layers (e.g., PAMI18). Finally, most of the methods but the first two in Table I rely on deep-learning approaches. A key aspect characterizing each method considering the positional information separately (from row 4, CVPR18), is the way they handle the fusion between the positional information and the visual content information corresponding to the video playback. As these two types of information are time series, those works all consider the use of deep recurrent networks (all use LSTM). However, whether the time features are first extracted from each time series independently, or whether the time series samples are first

concatenated then fed to a common LSTM, depends on the specific method. The positioning of the recurrent network in the whole architecture is the grouping criterion we have selected (col. 6) to order the rows the way they are (within each group, methods are ordered from the most recently published), thereby extracting 3 clusters of methods (corresponding to the group of rows in Table I):

- if the positional information is not explicitly considered, then no fusion is made and a single LSTM processes the content of the FoV: PAMI18;
- if only the current saliency map extracted from the content is considered to be fused with the estimated position predicted by an LSTM module, then fusion is made after the LSTM module: CVPR18 (see Fig. 3-Right);
- if the current saliency map extracted from the content is first concatenated with the current position information, then the LSTM module handles both pieces of information simultaneously: NOSSDAV17, ChinaCom18, MM18 (see Fig. 3-Left).

The architectures tackling this dynamic head motion prediction problem have hence three main objectives: (O1) extracting attention-driving features from the video content, (O2) processing the time series of position, and (O3) fusing both information modalities to produce the final position estimate. For concise representation and because we will focus on objectives (O2) and (O3) in Sec. IV and V, we depict the corresponding modules of methods MM18 and CVPR18 in Fig. 3. The existing methods are described more in detail next and those in bold are selected for comparison with the baselines presented in Sec. III.

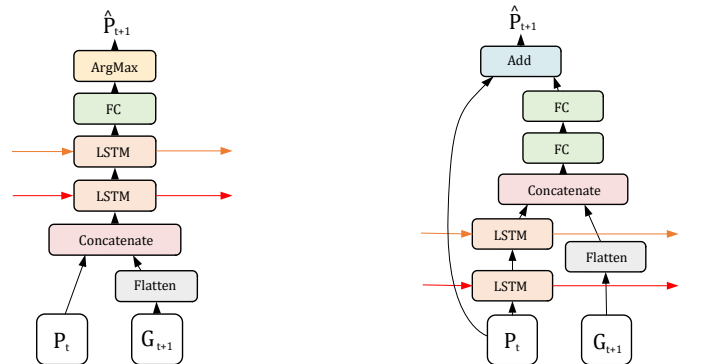


Fig. 3: The building blocks in charge of extracting time consistency and fusing positional (P_t) and information content (represented as saliency G_t after the saliency extractor module omitted in this scheme). Left: MM18 [9]. Right: CVPR18 [8]

C. Detailed description of methods selected for comparison

PAMI18: Xu et al. in [7] design a Deep Reinforcement Learning model to predict head motion. Their deep neural network only receives the viewer's FoV as a 42×42 input image, and has to decide to which direction and with which magnitude the viewer's head will move. Features obtained from convolutional layers processing each 360° frame cropped to the FoV are

| Reference | Objective | Prediction horizon | Dataset | Inputs | LSTM before/after fusion |
|------------------------|------------------|--------------------|--|--|--------------------------|
| PAMI18 [7] | head coordinates | 30ms | 76 videos, 58 users | frame cropped to FoV | N/A (no fusion) |
| IC3D17 [17] | head coordinates | 2s | 16 videos, 61 users | Pre-trained sal. in FoV | N/A (no fusion, no LSTM) |
| ICME18 [18] | tiles in FoV | 6s | 18 videos, 48 users | Position history, users' distribution | N/A (no LSTM) |
| CVPR18 [8] | gaze coordinates | 1s | 208 videos, 30+ users | Video frame, position history as coordinates | before |
| MM18 [9] | tiles in FoV | 2.5s | NOSSDAV17's dataset with custom pre-processing | Pre-trained sal., mask of positions | after |
| ChinaCom18 [10] | tiles in FoV | 1s | NOSSDAV17's dataset | Pre-trained sal., FoV tile history | after |
| NOSSDAV17 [11] | tiles in FoV | 1s | 10 videos, 25 users | Pre-trained sal., FoV position or tile history | after |

TABLE I: Taxonomy of existing dynamic head-prediction methods. References in bold are considered for comparison in Sec. III.

then fed into an LSTM to extract direction and magnitude. The training is done end-to-end. The prediction horizon is only one frame, i.e., 30ms. By only injecting the FoV, the authors make the choice not to consider the positional information explicitly as input. The PAMI18 architecture therefore does not feature any specific fusion module. The better performance of our position-only baseline shown in Sec. III questions this choice. **IC3D17**: The strategy presented by Aladagli et al. in [17] simply extracts saliency from the current frame with an off-the-shelf method, identifies the most salient point, and predicts the next FoV to be centered on this most salient point. It then builds recursively. We therefore consider this method to be a sub-case of PAMI18 to which we compare.

ICME18: Ban et al. in [18] assume the knowledge of the users' statistics, and hence assume more information than our case of study, which is to predict the user motion only based on the user's position history and the video content. A linear regressor is first learned to get a first prediction of the displacement, which it then adjusts by computing the centroid of the k nearest neighbors corresponding to other users' positions at the next time-step.

CVPR18: In [8], Xu et al. predict the gaze positions over the next second in 360° videos based on the gaze coordinates in the past second and current frame and on motion information. As depicted in Fig. 3-Right, the time series of past head coordinates is processed by a stack of two LSTMs. Spatial and temporal saliency maps are first concatenated with the RGB image, then fed to Inception-ResNet-V2 to obtain the "saliency features" denoted as G_{t+1} in Fig. 3-Right. They formulate the gaze prediction problem the same way as the head prediction problem. We therefore consider this architecture and compare it with our baselines for the original problem of gaze prediction, then consider this building block for the head prediction problem in Sec. V.

MM18: Nguyen et al. in [9] first construct a saliency model based on a deep convolutional network and named PanoSalNet. The so-extracted saliency map is then fed, along with the position encoded as a mask, into a doubly-stacked LSTM, as shown in Fig. 3-Left.

ChinaCom18: Li et al. in [10] present a similar approach

as MM18, adding a correction module to compensate for the fact that tiles predicted to be in the FoV with highest probability may not correspond to the actual FoV shape (having even disconnected regions). This is a major drawback of the tile-based approach as re-establishing FoV continuity may significantly impact final performance.

NOSSDAV17: Fan et al. in [11] propose two LSTM-based networks, predicting the likelihood that tiles pertain to future FoV. Positional information and visual features extracted from a pre-trained VGG-16 network are concatenated then fed into LSTM cells for the last n time-steps, to predict the head orientations in the future m time-steps. Similarly to MM18 and as depicted in Fig. 3, the building block of NOSSDAV17 first concatenates flattened saliency map and position, and feeds it to a doubly-stacked LSTM whose output is post-processed to produce the position estimate.

These four methods therefore make for a wide range of deep network architectural choices for the prediction problem at hand, where in particular the fusion problem (O3) defined above is each time handled differently. CVPR18 and MM18 are selected as representatives: handling the fusion before or after the recurrent (LSTM) unit, respectively. There is no pairwise comparison between any of the above works. Except for PAMI18 and MM18, none of the above articles came with publicly available code to reproduce the results. However, we could obtain all the datasets to compare with those methods (those not publicly available were kindly sent by the authors whom we have contacted).

III. COMPARISON AGAINST TWO BASELINES: NO-MOTION AND POSITION-ONLY

In view of comparing most recent proposals (PAMI18, CVPR18, MM18, ChinaCom18, NOSSDAV17) to a common reference, we first introduce a *no-motion baseline* and a *position-only baseline*. The latter is a sequence-to-sequence LSTM-based architecture which exploits the time series of past positions only, disregarding the video content. We obtain the striking result that every existing method considered, without any exception, performs worse than the no-motion baseline. By outperforming the no-motion baseline, we show

that our position-only baseline is able to establish state-of-the-art performance. Sec. IV will introduce a *saliency-only baseline*, which with the *position-only baseline* will then be the references to outperform by architectures attempting to leverage both the positional and content information. Lastly, we provide main implementation optimization of our *position-only baseline*.

A. Definition of the no-motion baseline

Different linear predictors can be considered as baselines. We consider here the simplest one which predicts no motion: $[\hat{\mathbf{P}}_{t+1}, \dots, \hat{\mathbf{P}}_{t+H}] = [\mathbf{P}_t, \dots, \mathbf{P}_t]$. Another possible baseline is to predict the same last motion recursively: $\hat{\mathbf{P}}_{t+1} = \mathbf{P}_t + (\mathbf{P}_t - \mathbf{P}_{t-1})$ and $\hat{\mathbf{P}}_{t+k} = \hat{\mathbf{P}}_{t+k-1} + (\hat{\mathbf{P}}_{t+k-1} - \hat{\mathbf{P}}_{t+k-2})$ for $1 < k \leq H$. As we will see, all existing methods trying to leverage both the video content and the position to predict future positions perform worse than the no-motion baseline, without exception. This harsh observation has triggered this work, and is sufficient to question the models, analyze their weaknesses and propose solutions to solve them.

B. Design of a competitive position-only baseline

We now present an LSTM-based predictor which considers positional information only. An LSTM enables non-linear shape of the motion and the memory effect due to inertia, as discussed in [8] (and confirmed in Fig. 7). We select a sequence-to-sequence (seq2seq) architecture because it has proven powerful at capturing complex dependencies and generating realistic sequences, as shown in text translation for which it has been introduced [19]. As depicted in Fig. 4, a seq2seq framework consists of an encoder and a decoder. The encoder receives the *historic window* input and generates an internal representation while the decoder receives the output of the encoder and progressively produces outputs by re-injecting the previous prediction as input for future time-steps. The re-injection loop is done as long as the *prediction window* indicates. The novelty is to define a refined baseline (not only a no-motion or linear predictor) processing the head coordinates only. This position-only baseline therefore enables to identify whether the existing methods actually outperform it when considering an extra information modality (the video content). We have optimized the position-only baseline (in terms of loss definition, history input length and type of output, as detailed in Sec. III-D) in order to obtain as much prediction accuracy as possible with the positional modality only.

C. Results

We now present the comparisons of the state-of-the-art methods presented in Sec. II-B with the no-motion and position-only baselines defined above. We report the exact results of the original articles, along with the results of our baselines, the position-only baseline being trained and tested on the exact same train and test subsets of the original dataset as the original method (there is no training for the no-motion baseline). The test metrics (related to predicting head or gaze positions, or FoV tiles) are those from the original articles,

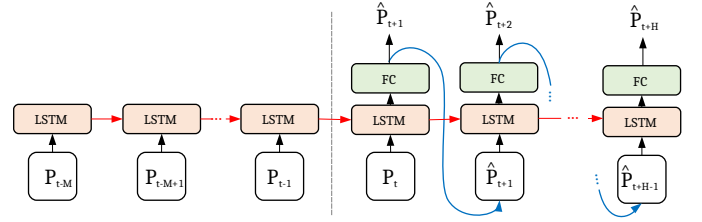


Fig. 4: Our seq2seq-based *position-only baseline*. From the vertical line, the extension to the right is called *prediction window* and the extension to the left is called *historic window*.

so are the considered prediction horizons. The experimental setup and dataset of each assessed method are detailed in the supplemental material [20].

Results for PAMI18 are shown in Table II, for CVPR18 in Fig. 5-Left, for MM18 in Fig. 5-Right, for ChinaCom18 in Table III and for NOSSDAV17 in Table IV. All perform worse than both our no-motion and position-only baselines. These striking results call for a thorough analysis of the current architectures investigated for head motion prediction, which we address in the next sections.

We understand that the harshness of our findings might genuinely raise some suspicion as to the validity of our comparisons. This is why, in our concern for reproducibility, we commit to make the entire code used for all the experiments throughout the article publicly available. Let us also mention that these findings echo those of Martinez et al. in [21], who recently showed, in another application domain, that simple baselines outperform all the existing deep architectures for the problem of 3D-skeleton pose prediction.

Finally, for the sake of completeness, we summarize below information on the metrics of each experiment.

• **NOSSDAV17** [11] considers the following metrics:

- *Accuracy*: ratio of correctly classified tiles to the union of predicted and viewed tiles.
- *Ranking Loss*: number of tile pairs that are incorrectly ordered by probability normalized to the number of tiles.
- *F-Score*: harmonic mean of *precision* and *recall*, where *precision* is the ratio of correctly predicted tiles by the total number of predicted tiles, and *recall* is the ratio of correctly predicted tiles by the number of viewed tiles.

Let us point out here that the data are not represented equally, as more tiles pertain to class 0 (tile \notin FoV) than to class 1 (tile \in FoV) owing to the restricted size of the FoV compared to the complete panoramic size. If we predict all the tiles systematically in class 0, the accuracy already gets to 83.86%. The accuracy is indeed known to be a weak metric to measure the performance of such unbalanced datasets. A similar issue has been found when using the binary cross entropy as loss function of an unbalanced dataset [22].

• **PAMI18** [7] uses as metric the Mean Overlap (MO) defined as:

$$MO = \frac{A(FoV_p \cap FoV_g)}{A(FoV_p \cup FoV_g)}$$

Where FoV_p is the predicted FoV, FoV_g is the ground truth FoV, and $A(\cdot)$ is the area of a panoramic region.

- **CVPR18** [8] uses the Intersection Angle Error IAE for each gaze point (θ, φ) and its prediction $(\hat{\theta}, \hat{\varphi})$, defined as $IAE = \arccos(\langle P, \hat{P} \rangle)$, where P is the 3D coordinate in the unit sphere:

$P = (x, y, z) = (\cos(\theta)\cos(\varphi), \cos(\theta)\sin(\varphi), \sin(\theta))$. Let us mention that CVPR18 also considers a position-only baseline. However, ours appears stronger, likely due to the seq2seq architecture. We readily apply our different predictors on the gaze data available in the CVPR18-dataset.

- **MM18** [9] takes the tile with the highest viewing probability as the center of the predicted viewport, and assigns it and all the neighboring tiles that cover the viewport, with label 1. Tiles outside the viewport are assigned 0. Then, the score is computed on these labels as $IoU = TP/TT$, the intersection between prediction and ground-truth of tiles with label 1 (TP) over the union of all tiles with label 1 in the prediction and in the ground-truth (TT).

- **ChinaCom18** [23] uses the Accuracy and F-Score on the labels assigned to each predicted tile.

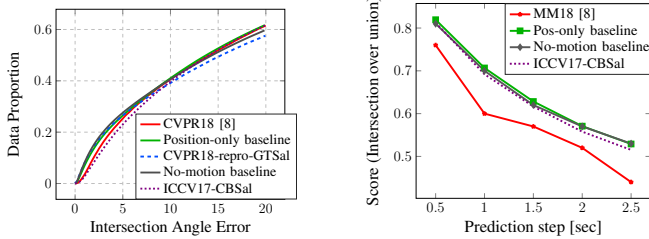


Fig. 5: Left: Comparison with CVPR18 [8]. Right: Comparison with MM18 [9]. CVPR18-repro is the result of our reproduction of CVPR18 model. The model ICC17-(Content-Based) Saliency is discussed in Sec. VI-C.

D. Important implementation choices for training the position-only baseline

Deep network setup: This model was developed using *Keras* [24] and *Scikit-Learn* [25]. We used Adam optimization algorithm [26] with a learning rate of 0.0005, and we select the best performing model after training for 500 epochs to produce each of the results in this work. The batch size was set to 128.

Dataset: The next figures are generated with the MMSys18-dataset [27], later presented in Sec. IV. In this dataset we have a set of users U and a set of videos V . In the validation stage, there is no intersection between the subsets $U_{train} \times V_{train}$ and $U_{test} \times V_{test}$. This way we make sure that the network does not exploit any information about the behavior of each user, or particular features of a video.

Loss function determination: The tracking problem on a sphere can be assessed by different distances between the predicted and ground-truth points. Given two points on the surface of the unit sphere $P_1 = (\theta_1, \varphi_1)$ and $P_2 = (\theta_2, \varphi_2)$, where θ is the longitude and φ is the latitude of the point, possible distance are:

- **Mean squared error:** $MSE = ((\theta_1 - \theta_2)^2 + (\varphi_1 - \varphi_2)^2)/2$
- **Angular error:**

$$AngErr = \sqrt{\arctan 2(\sin(\Delta\theta)/\cos(\Delta\theta))^2 + (\varphi_1 - \varphi_2)^2}$$

where $\Delta\theta = \theta_1 - \theta_2$.

- **Orthodromic distance:** $OrthDist =$

$$\arccos(\cos(\varphi_1)\cos(\varphi_2)\cos(\Delta\theta) + \sin(\varphi_1)\sin(\varphi_2))$$

The latter two are able to handle the periodicity of the latitude, which the first one cannot. The difference between *angular error* and *orthodromic distance* is that the latter computes the distance on the surface of the sphere, while the *angular error* computes the error of each angle independently. Fig. 6-Left shows that the relationship between the *angular error* and the *orthodromic distance* is not bijective, and importantly that the *orthodromic distance* varies rather logarithmically with the *angular error*. The green dots are the points at the pole $P_{pole} = (\theta, \frac{\pi}{2})$ with $\theta \in [-\pi, \pi]$. We observe how the *angular error* as loss function penalizes points that are in the same spot in the surface of the sphere but with different angles (the pole’s latitude described a unique point for any longitude). The largest difference in *orthodromic distance* is the antipodal point $P_{antipode} = (\pi, 0)$, while for the *angular error* the largest distance occurs at the poles $P_{pole} = (\pi, \frac{\pi}{2})$. This is shown by the red dots which are all the points $\hat{P} = (\pi, \varphi)$ with $\varphi \in [0, \frac{\pi}{2}]$. Let us note how the *angular error* increases when the *orthodromic distance* decreases for these points. In general, for a point $P = (\theta, \varphi)$ the *orthodromic distance* decreases and the *angular error* increases when we set θ fixed and move to either of the poles by varying φ from 0 to π (or $-\pi$). Finally, owing to its fitness to the tracking problem on the unit sphere with latitude and longitude as inputs, we choose the *orthodromic distance* as the train and test metric with the input formatted with longitude and latitude (θ, φ) of the FoV’s center.

Prediction of orientation change ΔP_t : Fig. 6-Right shows that predicting the motion instead of the absolute position remedies a temporary increase in error for short-term prediction. This has been already identified in the case of 3D-skeleton pose prediction in [21] and CVPR18 [8] for gaze prediction.

How much historic information to use?: Fig. 7-Left shows that the error progressively reduces when increasing the historic window up to 1 sec. Beyond this value, no further improvement is obtained.

Generated trajectories: We finally illustrate the type of head trajectories generated with our baseline. As shown in Fig. 7-Right, the network is able to learn non-linear realistic trajectories ($[-180^\circ, 180^\circ]$ is projected onto $[0, 1]$, note that the jump from 1 to 0 only reflects the crossing from 180° to -180°). We also mention here that we observe the predicted motion tends to vanish over time. This is a well-known drawback of the l_1 -type losses, where the network copes with uncertainty increasing over time by averaging over possible

| Method | KingKong | SpaceWar2 | StarryPolar | Dancing | Guitar | BTSRun | InsideCar | RioOlympics | SpaceWar | CMLauncher2 | Waterfall | Sunset | BlueWorld | Symphony | WaitingForLove | Average |
|------------------------|--------------|--------------|--------------|--------------|--------------|--------------|--------------|--------------|--------------|--------------|--------------|--------------|--------------|--------------|----------------|--------------|
| PAMI18 [7] | 0.809 | 0.763 | 0.549 | 0.859 | 0.785 | 0.878 | 0.847 | 0.820 | 0.626 | 0.763 | 0.667 | 0.659 | 0.693 | 0.747 | 0.863 | 0.753 |
| No-motion baseline | 0.974 | 0.963 | 0.906 | 0.979 | 0.970 | 0.983 | 0.976 | 0.966 | 0.965 | 0.981 | 0.973 | 0.964 | 0.970 | 0.968 | 0.978 | 0.968 |
| Position-only baseline | 0.983 | 0.977 | 0.930 | 0.984 | 0.977 | 0.987 | 0.982 | 0.976 | 0.976 | 0.989 | 0.984 | 0.973 | 0.979 | 0.976 | 0.982 | 0.977 |
| ICCV17-CBSal | 0.974 | 0.964 | 0.912 | 0.978 | 0.968 | 0.982 | 0.974 | 0.965 | 0.965 | 0.981 | 0.972 | 0.964 | 0.970 | 0.969 | 0.977 | 0.968 |

TABLE II: Comparison with PAMI18 [7]: Mean Overlap scores of FoV prediction. The model ICC17-(Content-Based) Saliency is introduced in Sec. VI-C.

| | No-motion baseline | | Position-only baseline | | ChinaCom18 | |
|-----------------|--------------------|---------|------------------------|---------------|------------|---------|
| | Accuracy | F-score | Accuracy | F-score | Accuracy | F-score |
| Hog Rider | 96.29% | 0.8858 | 96.97% | 0.9066 | 77.09% | 0.2742 |
| Driving with | 95.96% | 0.8750 | 96.59% | 0.9843 | 77.34% | 0.2821 |
| Shark Shipwreck | 95.23% | 0.8727 | 96.12% | 0.8965 | 83.26% | 0.5259 |
| Mega Coaster | 97.20% | 0.9144 | 97.71% | 0.9299 | 88.90% | 0.7011 |
| Roller Coaster | 96.99% | 0.9104 | 97.50% | 0.9256 | 88.28% | 0.6693 |
| Chariot-Race | 97.07% | 0.8802 | 96.91% | 0.9056 | 87.79% | 0.6040 |
| SFR Sport | 96.00% | 0.8772 | 96.91% | 0.9054 | 89.29% | 0.7282 |
| Pac-Man | 96.83% | 0.8985 | 97.16% | 0.9089 | 87.45% | 0.6826 |
| Peris Panel | 95.60% | 0.8661 | 96.54% | 0.8947 | 89.12% | 0.7246 |
| Kangaroo Island | 95.35% | 0.8593 | 96.54% | 0.8954 | 82.62% | 0.5308 |
| Average | 96.15% | 0.8840 | 96.90% | 0.9063 | 72.54% | 0.5155 |

TABLE III: Comparison with ChinaCom18 [10]

| Method | Accuracy | F-Score | Rank Loss |
|------------------------|---------------|-------------|-------------|
| NOSSDAV17-Tile [11] | 84.22% | 0.53 | 0.19 |
| NOSSDAV17-Orient. [11] | 86.35% | 0.62 | 0.14 |
| No-motion baseline | 95.79% | 0.87 | 0.10 |
| Position-only baseline | 96.30% | 0.89 | 0.09 |
| ICCV17-CBSal | 95.48% | 0.85 | 0.15 |

TABLE IV: Comparison with NOSSDAV17: Performance of Tile- and Orientation-based networks of [11] compared against our position-only baseline. The model ICC17-(Content-Based) Saliency is discussed in Sec. VI-C.

modes, generating vanishing motion or blur, as exhibited for segmentation prediction in [28] and 3D-skeleton pose prediction in [21] (possibly remedied with adversarial losses, out of the scope of this article).

IV. ROOT CAUSE ANALYSIS: THE DATA IN QUESTION

We have shown that all existing methods which try to leverage both positional information and video content to predict future positions perform worse than a simple baseline assuming no motion, which in turn can be outperformed by our

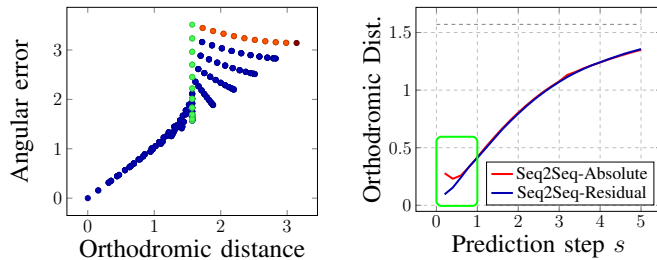


Fig. 6: Left: Relationship between orthodromic distance and angular error. Right: Performance of the network when predicting absolute fixation position P_t and when predicting fixation displacement ΔP_t using a residual network.

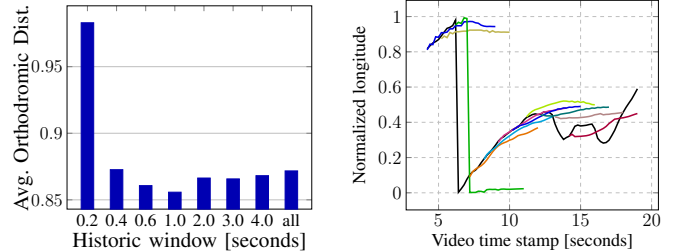


Fig. 7: Left: Impact of the historic-window size. Right: Ground truth longitudinal trajectory (for video “Diner”, user 4) is shown in black, colors are the non-linear trajectories predicted by the position-only baseline from each time-stamp t .

position-only baseline which considers only positional information. This section and the next (Sec. V) aim at identifying the reasons for such consistently worse performance of the existing approaches. We first list and classify the possible causes, related to the data and to the deep network.

- Possible causes due to the data are:

Q1 Even if they degrade elsewhere, do the methods get better results than the baselines for some parts of the trajectory, i.e., despite the results averaged over the entire trajectory being worse?

Q2 Do the datasets (made of videos and motion traces) match the design assumptions the methods build on?

- In view of the superiority of our seq2seq position-only baseline, possible causes due the deep network are:

Q3 Can arranging the building block (combining position and content information and exploiting their time consistency, as shown in Fig. 3) of each method into another auto-regressive framework improve the results?

Q4 Is the building block of each method unable to exploit part of the available information?

We then endeavor to test each one: those related to the data are analyzed in this section, while those related to the deep network (architecture and training choices) are analyzed in Sec. V. We report the answer to each question after their analysis. To investigate the first set of possible causes related to the dataset, we make the following breakdown of the assumptions at the core of the existing architectures attempting to leverage the knowledge of position history and video content:

- [A1] future positions are correlated with the position history;
 - [A2] future positions are correlated with the visual content.
- We now attempt to identify whether these correlations hold in the considered datasets.

A. Assumption 1: Correlation with position history

Correlation A1 corresponds to motion continuity (inertia). Fig. 8 represents the Cumulative Distribution Function (CDF) of the displacement withing each prediction horizon $H = 0.2s, \dots, 15s$ for the datasets considered in PAMI18, CVPR18, MM18 and NOSSDAV17. Hence, each point (x, y) on a curve represents the fraction y of samples (in the users' traces) for which the displacement with Hs has been less than x degrees. If we consider a FoV to be about 100° wide [11], these figures show how many seconds it takes for the FoV to shift by at least half of its width for half of the samples. It takes respectively at least 5 seconds for all but CVPR18 for which it takes about 2s, and for the MMSys18-dataset from [27] and introduced next. Over the considered forecast window in each of these works, the FoV has shifted by half of its width for less than 0.5%, 5%, 5% and 7% of the samples, respectively. These datasets are therefore characterized by very slow motion, which means that correlation A1 is strong. Another element supporting this observation is the best performance obtained by our baseline exploiting position only (see Sec. III above).

B. Assumption 2: Correlation with the video content

Before analyzing whether, and for which settings (datasets, prediction horizons), assumption A2 holds and impacts the average performance, we first look at whether A2 holds and can impact the performance of existing methods for parts of the trajectories.

Low-scale analysis (intra-trajectory):

The existing methods taking the content into account show performance, averaged over all videos and users' trajectories, worse than the no-motion baseline. Despite this average performance, let us first look at whether these methods can outperform the baselines for some parts of the trajectory where the position history only is not sufficient to predict future positions, i.e., where baselines are likely to give larger errors. To carry out such a quantitative analysis, we first define the *difficulty of prediction* as breaking points of the smooth inertia-driven trajectory, which changes somewhat abruptly owing to the attention being caught by the content. We therefore choose to quantify this difficulty with the absolute value of the second derivative of the trajectory (related to the radius of curvature). The prediction around these points therefore requires the analysis of the content and our baselines are therefore expected to perform worse than in easier trajectory regions. This is akin to the *Average non-linear displacement error* considered in [29] to assess how much the network can disrupt the trajectory based on data external to the trajectory inertia. To obtain detailed results (for each instant of time of each user and video pair), we re-implement CVPR18 with the exact same architectural and training parameters as those described in the article [8]. The curve CVPR18-repro in Fig. 5 shows we obtain similar results on their original dataset, which confirms the validity of our re-implementation. Fig. 9 depicts the distribution of the prediction difficulty in the left-hand side. We observe in the right-hand side that, for any of the difficulty range, the method is not able to improve the prediction over the baselines.

Answer to Q1: No, the methods do not get better result than the baseline on some difficult parts of the trajectory.

High-scale analysis (average performance):

The rest of the section analyzes whether assumption A2 holds and impacts the performance over the entire trajectory duration, and for which settings (datasets, prediction horizons). Let us first provide characteristics of the human attention in VR identified recently. It has been recently shown in [30] and [31] that, when presented with a new VR scene (the term "scene" is defined by Magliano and Zacks in [32] as a period of the video between two edits with space discontinuity), a human first goes through an exploratory phase that lasts for about 10 to 15s ([31, Fig. 18], [30, Fig. 2]), before settling down on so-called Regions of Interest (RoIs), that are salient areas of the content. The duration and amplitude of exploration, as well as the intensity of RoI fixation, depends on the video content itself. Almquist et al. [31] have identified the following main video categories for which they could discriminate significantly different users' behaviors: *Exploration*, *Static focus*, *Moving focus* and *Rides*. In *Exploration* videos, the spatial distribution of the users' head positions tends to be more widespread, making harder to predict where the users will watch and possibly focus on. *Static focus* videos are made of a single salient object (e.g., a standing-still person), making the task of predicting where the user will watch easier in the focus phase. In *Moving focus* videos, contrary to *Static focus* videos, the RoIs move over the sphere and hence the angular sector where the FoV will be likely positioned changes over time. *Rides* videos are characterized by substantial camera motion, the attracting angular sector being likely that of the direction of the camera motion.

To analyze Assumption A2 and assess how much gain can the consideration of the content bring to the prediction, we define a family of so-called saliency-only baselines.

First, to be independent from the imperfection of any saliency predictor fed with the visual content, we consider the so-called ground-truth saliency, that is the heat map (2D distribution) of the viewing patterns, obtained at each point in time from the users' traces.

Second, we extract different trajectory predictors from the heat map. Each is indexed by variable K . For each prediction step $t+s$, for all t , for all $s \in [0, H]$, the saliency-only baseline predictor predicts $\hat{\mathbf{P}}_{t+s}$ as the position of the peak of the heat map at $t+s$ closest to \mathbf{P}_t , amongst the K highest peaks.

Each predictor can be considered as an upper-bound on the error that the best predictor optimally combining position and content modality could get. Different values of K (set to 1, 2 and 5 in the revised version) therefore enable to have refined upper-bounds for each prediction step $t+s$, $\forall s \in [0, H]$, considering the lowest upper-bound as an estimate of the best prediction possible for each prediction step s . The saliency-only baselines for $K = 1, 2$ and 5 can be seen in Fig. 10 and 11. From Fig. 12, we only represent the minimum of these upper-bounds for every s (shown in red in Fig. 12), and refer to it as simply *Saliency-only baseline*.

Analyzing Q2 aims at identifying how does this (non-)relevance of the content evolve when the prediction step increases. From the answer to Q1, we set the prediction

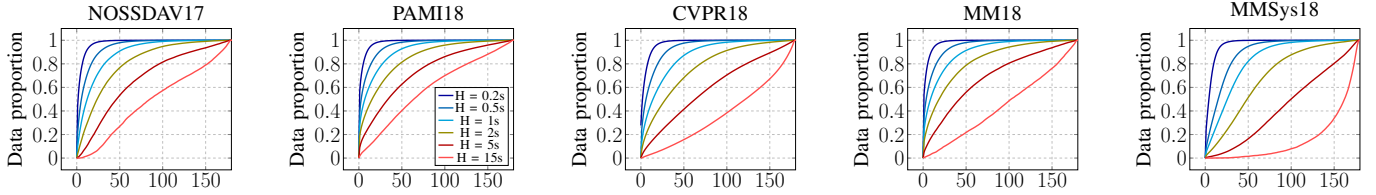


Fig. 8: From left to right: Motion distribution of the 4 datasets used in NOSSDAV17, PAMI18, CVPR18 and MM18, respectively. The last on the right is the distribution of the MMSys18-dataset from [27] and considered in the sequel. The x-axis corresponds to the motion from position t to position $t+H$ in degrees.

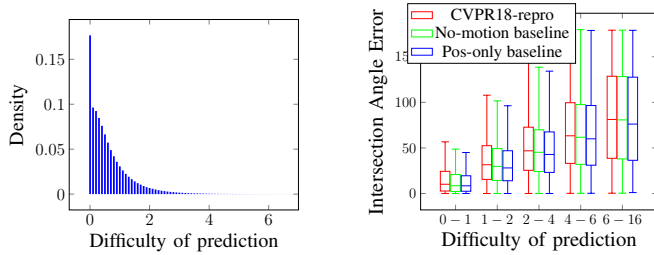


Fig. 9: Left: Distribution of difficulty in the dataset. Right: Error as a function of the difficulty for CVPR18.

horizon $H = 5s$, so that both short-term where the motion is mostly driven by inertia from t , and long-term where the content saliency impacts the trajectory, are likely to be covered. We confirm this in the next results.

We analyze Q2 on the datasets used in NOSSDAV17, MM18, CVPR18 and PAMI18. We also consider an additional dataset, referred to as MMSys18-dataset, presented by David et al. in [27]. It is made of 19, 360° videos of 20 seconds, along with the head and eye gaze recording of 57 participants starting each at a random angular position. The authors show that the exploration phase in their videos lasts between 5 and 10s, and show that after this initial period, the different users' positions have a correlation coefficient reaching 0.4 [27, Fig. 4]. This dataset is made of 12 Exploration videos, 4 Static focus videos (Gazafisherman, Sofa, Mattswift, Warship), 1 Moving focus video (Turtle) and 2 Ride videos (Waterpark and Cockpit).

Fig. 10, 11, 12 and 13 depict the prediction error for prediction steps $s \in [0, H = 5s]$, obtained with the position-only and saliency-only baselines. We remind that each point is an average over all the users and all time-stamp $t \in [T_{start}, T]$, with T the video duration and $T_{start} = 6s$ from now on. The same phenomenon can be observed on all the datasets: by analyzing the lowest of the saliency-only baselines for every prediction step s (saliency-only baseline in red in Fig. 12), we can see that the upper-bound on the error of the best predictor is higher than the position-only baseline for s lower than 2 to 3 seconds, which means that there is no guarantee that the prediction error can be lowered by considering the content in this range of prediction step. After 2 to 3s, on non-Exploration videos, we can see that relevant information can be exploited from the heat maps to lower the prediction error compared to the position-only baseline.

When we isolate the results per video type, e.g., in Fig. 10, for Exploration (PortoRiverside, PlanEnergyBioLab), a Ride

(WaterPark) a Static focus (Warship) and a Moving focus (Turtle) videos, we observe that the saliency information can significantly help predict the position for prediction steps beyond 2 to 3 seconds, when the initial inertia at time t gets less relevant than the saliency baseline.

Answer to Q2: Making the assumption that the heat maps can be estimated from the content, we conclude on Q2 by stating that considering the content in the prediction can significantly help for non-Exploration videos if the prediction horizon is longer than 2 to 3s, but there is no guarantee it can significantly or easily help for shorter horizons. We show that the assumption that information exploitable from the heat maps can be also be extracted from the content, is verified in Sec. VI.

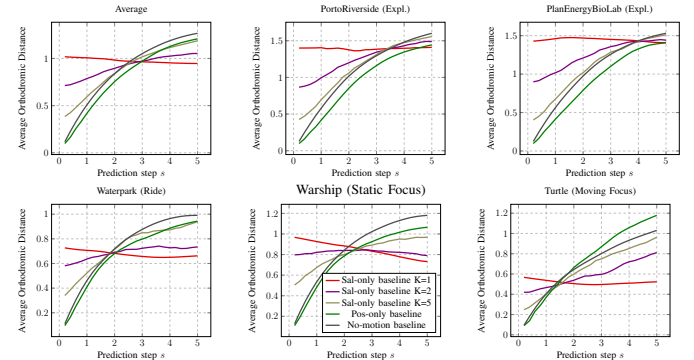


Fig. 10: Average error with the no-motion, position-only baselines, most salient object and point (saliency-only baseline). Top left: Average results on all 5 test videos. Rest: detailed result per test video in MMSys18 dataset.

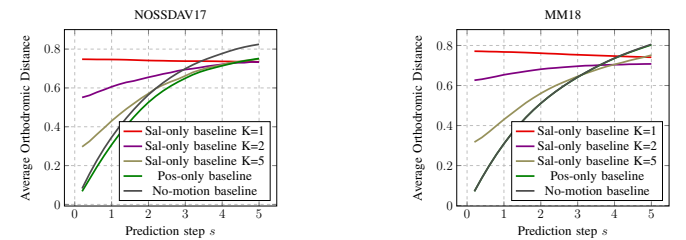


Fig. 11: Average error with the no-motion, position-only and saliency-only baselines on the datasets of NOSSDAV17 and MM18.

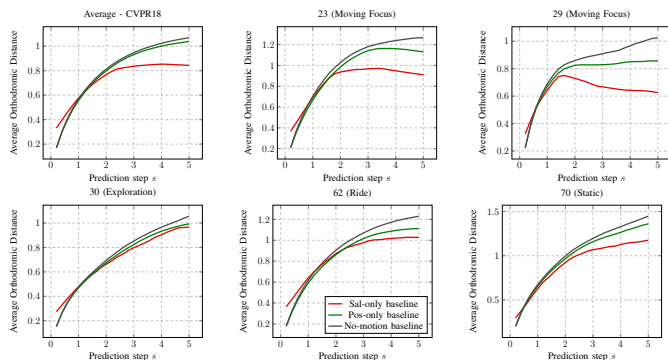


Fig. 12: Average error with the no-motion, position-only and saliency-only baselines on some videos on the dataset of CVPR18.

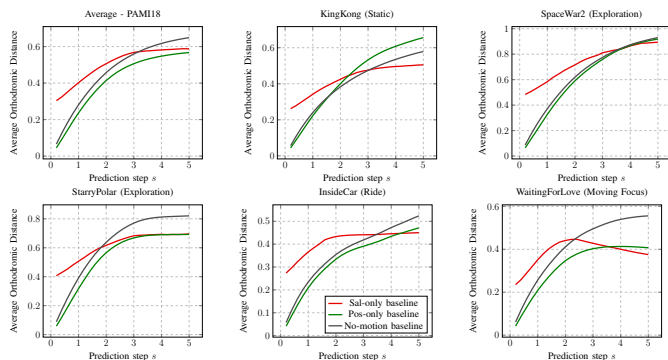


Fig. 13: Average error with the no-motion, position-only and saliency-only baselines on some videos on the dataset of PAMI18.

V. ROOT CAUSE ANALYSIS: THE ARCHITECTURES IN QUESTION

We have hence analyzed whether and when do the design assumptions of existing methods hold. In this section, we analyze their architecture and training choices to successively answer each of the questions introduced in Sec. IV:

- Q3 Can arranging the building block (i.e. combining position with content information and exploiting their time coherence, as shown in Fig. 3) of each method into another auto-regressive framework improve the results?
- Q4 Is the building block of each method unable to exploit part of the available information?

A. Common evaluation settings

Prediction horizon: From the previous discussion, we consider the problem of predicting head positions over a longer prediction horizon than the existing methods, namely 0 to $H = 5$ seconds. This way, both short-term where the motion is mostly driven by inertia at t , and long-term where the content saliency impacts the trajectory, are covered.

Dataset: Given the properties of MMSys18-dataset, where users move significantly more (see Fig. 8) and which is made of both videos where the content is not helpful for prediction, and videos where the content gets helpful after a

certain horizon, we select this dataset for the next experiments investigating the architectures. In particular, we draw a new dataset out of MMSys18-dataset, selecting the 10 train and 5 test videos making sure that the sets are balanced between videos where the content is helpful (Static focus, Moving focus and Rides) and those where it is not (Exploration). Specifically, the train set is made to comprise 7 Exploration videos, 2 Static Focus and 1 Ride, while the test set has 2 Exploration, 1 Static focus, 1 Moving focus and 1 Ride videos. This number of videos is equivalent to the dataset considered in MM18, ChinaCom18 and NOSSDAV17 (10). This dataset is therefore challenging but also well fitted to assess prediction methods aiming to get the best out of positional and content information.

B. Impact of the dataset on the original methods

Let us recall the three main objectives a prediction architecture must meet, as stated in Sec. II-B: (O1) extracting attention-driving features from the video content, (O2) processing the time series of position, and (O3) fusing both information modalities to produce the final position estimate. As we have identified in Sec. III that all existing works perform worse than our baseline exploiting position only, we focus now on showing whether each representative building block (MM18 and CVPR18, see Fig. 3) can perform (O2) and (O3), leaving the assessment of (O1) for Sec. VI. Therefore, to avoid any impact of the difference in their saliency extractors, we replace the output of the latter with the ground truth saliency map, that is the heat map obtained for each time-stamp by all the other users' positions. With this modification, we re-implement CVPR18 with the exact same architectural and training parameters as those described in the article [8]. The curve CVPR18-repro in Fig. 5 shows that we obtain similar results on their original dataset, which confirms the validity of our re-implementation. For MM18, we use the code provided by the authors in [33]. We however retain the orthodromic distance as the test metric (which is also used to train the position-only baseline).

Results: Fig. 14 shows the average error (orthodromic distance) averaged over all videos and users in the test set (disjoint from any of the videos or users in the train set), for each time-step in a prediction horizon H of 5 seconds. It depicts the performance of the original architectures CVPR18 and MM18 reproduced (tagged with -repro in the legend) and of all three baselines (no-motion, our position-only and saliency-only baselines introduced in Sec. III and IV, respectively). We observe that both original methods CVPR18 and MM18, despite being run on well-picked dataset and prediction horizons (see Sec. IV), are still outperformed by the no-motion baseline, and cannot gain any accuracy from the saliency, even in the prediction range where it proves useful (after about 3s).

C. Analysis of the auto-regressive framework

We make three modifications to CVPR18 and MM18 (shown in Fig. 3), which we refer to as CVPR18-improved

and MM18-improved, respectively. **First**, as for our position-only baseline, we consider here also a seq2seq auto-regressive framework to predict over longer prediction windows. We therefore embed each of these MM18 and CVPR18 building blocks into the seq2seq framework. It corresponds to replacing every LSTM cell in Fig. 4 with the building block represented in Fig. 3-Right. **Second**, instead of training with orthodromic distance as loss function as in Sec. III, we train with the MSE based on 3D Euclidean coordinates $(x, y, z) \in \mathbb{R}^3$. This helps the convergence with a seq2seq framework handling content, which is likely due to the removal of the discontinuity of having to use a modulo after each output in the training stage when Euler angles are considered (to compute the orthodromic distance). With 3D Euclidean coordinates, the projection back onto the unit sphere is made only at test time. We however retain the orthodromic distance as the test metric (which is also used to train the position-only baseline). **Third**, instead of predicting the absolute position as done by MM18, we predict the displacement (motion). This corresponds to having a residual connection, which helps reduce the error in the short-term, as mentioned in Sec. III-D. Specifically for the MM18 block, we have also changed (1) the saliency map that we grow from 16×9 to 256×256 , and (2) the output, i.e. the center of the FoV, which is defined by its (x, y, z) Euclidean coordinates. The output was an image in [9], requiring then to extract the pixel with the highest value as an estimate of the center of the FoV.

Results: Fig. 14 also depicts our improved versions. Both CVPR18-improved and MM18-improved perform better than their original counterparts. However, it is noticeable that only CVPR18-improved is able to outperform our position-only baseline for long-term prediction, approaching the saliency-only baseline. CVPR18-improved is also able to stick to the same performance as the position-only baseline for short-term prediction. Importantly, this latter result suggests that it is better to split the module in charge of the fusion objective (O3) from that in charge of extracting the motion inertia (O2), and not having these two objectives being handled by the same recurrent unit, as in MM18. This appears to prevent from reaching the performance of the position-only baseline. We may hypothesize that such recurrent network has more difficulty discriminating position from content when fed with the concatenation of both.

Answer to Q3: Yes, the seq2seq auto-regressive framework is crucial for efficient long-term prediction. Note that the seq2seq allows to use a same architecture for predicting over the entire range of the prediction horizon, without training for each specific prediction step.

Answer to Q4: From the above explanation, the building block of CVPR18 is better fitted to the prediction problem.

Fig. 15 provides the detailed results of the best performing architecture, CVPR18-improved, over the different videos in the test set, associated with their respective category identified in [31]. While the average results show reasonable improvement towards the saliency-only baseline (we recall it is the ground-truth saliency and the network has been trained to best perform in average over all videos), the error differences between the saliency-only baseline and CVPR18-improved are

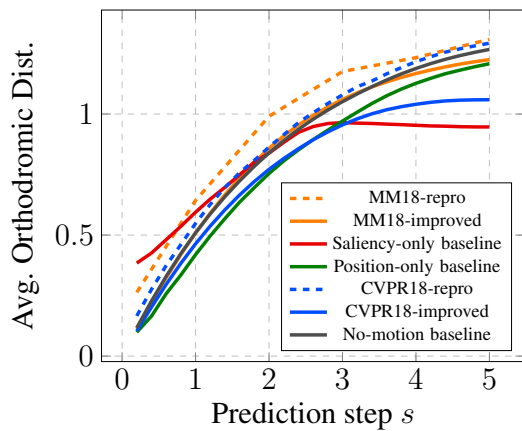


Fig. 14: Average error when predicting with the original and improved models of MM18 and CVPR18 compared with the position-only and saliency-only baselines.

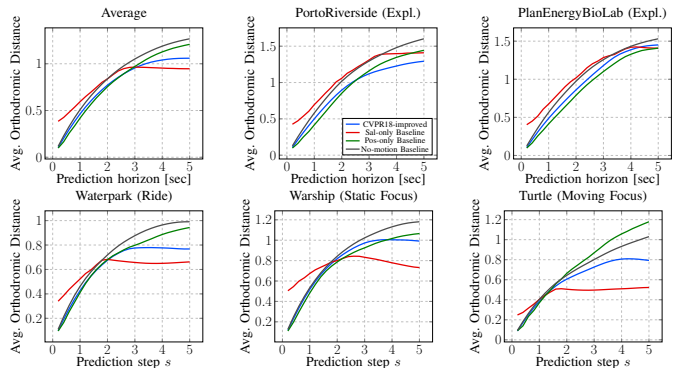


Fig. 15: Average orthodromic distance versus prediction window. Results of the improved CVPR18 architecture. Top left: average results on all test videos. Rest: detailed result for each type of test video.

dissimilar across the video categories. There is therefore room for improvement of deep architectures for this problem, a possible direction being a better learning of the video category.

VI. INTRODUCING BACK THE CONTENT-BASED SALIENCY

We have shown in Sec. IV that on Focus-type videos the video content can inform the head prediction better than the past positions for prediction horizons longer than about 3s. Sec. V above has shown that a seq2seq assembly of a deep building block featuring a recurrent cell (such as an LSTM) dedicated to processing the time series of positions, later fused with the content information, provides best performance (reaches a trade-off between position-only and saliency-only baselines). To carry out this last analysis of the architectures that are meant to (O2) extract time consistency and (O3) fuse information modalities, we prevented the specific choice of saliency extractor to impact the result by instead considering the ground-truth saliency maps obtained from the users' traces. In this section, we re-introduce the content-based saliency. Our goal is not to find the best saliency extractor, but instead to uncover the impact of less accurate saliency information onto

the architecture’s performance. We consider PanoSalNet [33], [9] in the remainder of this section. As expected, the heat map prediction can be substantially degraded compared to the ground-truth, but the most important finding is that the best architecture so far, CVPR18-improved, is not able to handle this noisy saliency without substantially degrading away from the position-only baseline. We carry out the analysis of the architectural reasons for this phenomenon, which leads us to propose a new architecture and show that the recurrent processing of the content information enables to smooth and improve the performance. We finally perform an ablation study to identify the essential components of this architecture.

A. Saliency extractor

The architecture of PanoSalNet is composed by nine convolution layers, the first three layers are initialized with the parameters of VGGNet[34], the following layers are first trained on SALICON[35], and finally the entire model is re-trained on 400 pairs of video frames and saliency maps in equirectangular projection.

B. Results of CVPR18-improved and analysis

Fig. 16 shows how does our architecture CVPR18-improved perform when fed with the Content-Based (CB) saliency (obtained from PanoSalNet) compared with the case it is fed with the Ground-Truth (GT) saliency.

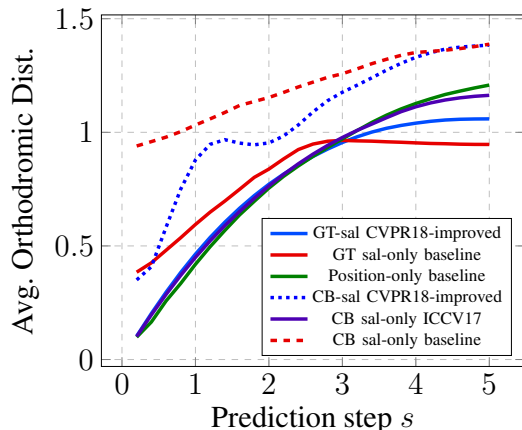


Fig. 16: Error for different prediction horizons for the models trained with Content-based (CB) Saliency compared with the models trained with Ground-truth (GT) saliency.

We first observe the general degradation using the CB saliency, compared with the GT saliency: we see in Fig. 16 that the CB saliency baseline (dashed red line) is much less accurate than the GT saliency baseline (solid red line). Architecture CVPR18-improved has difficulties to deal with the less relevant information to get, at least, as good a performance as the position-only baseline. Fig. 17-Left shows how the training convergence is indeed impaired in this case. Let us attempt to explain this degradation by first analyzing how does CVPR18-improved work when fed with the ground-truth saliency. The following is a tentative analysis which leads to proposing a better-performing architecture as we shall see,

and corroborates with an ablation study in the next section. We refer to Fig. 3-Right. In the seq2seq architecture, the weights of the Fully Connected (FC) layers (after the LSTM cell) are the same for all the prediction time-steps $s \in [0, H]$. It is therefore the only presence of the LSTM processing the time series of positions which allows to vary the input of the first FC layer over the different prediction time-steps. The amplitude of the LSTM outputs therefore varies over time, while the ground-truth saliency fed into the first FC layer can remain stable over time: the FC layers can learn to weigh the same way inputs from both modalities over time; yet the varying input coming from the LSTM makes the end result of prediction vary over time, the inertia being given more prevalence for the first time-steps, then outweighed by the saliency. However when replacing the ground-truth saliency with the content-based saliency, the saliency map is now much less correlated with the prediction objective, and hence acts as noise preventing to reach the performance of the position-only baseline, particularly in the first prediction steps. To understand the reason why the two FC layers after the concatenation are not able to learn the function they should, we have first verified if the CVPR18 network, still trained end-to-end, but without visual input, trains well to a point where the performance of our position-only baseline is reached. Once verified, we have then considered this same architecture but generating inputs of uniform noise to the fuse layer to emulate noised saliency: Fig. 17-Right shows the degradation in convergence speed when we increase the number of noisy inputs.

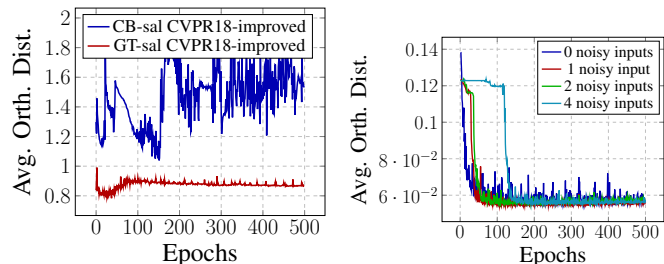


Fig. 17: Left: Evolution of the validation metric while training the networks for 500 epochs, when using the content-based (CB) or ground-truth (GT) saliency for CVPR18-improved. Right: Evolution of the validation metric (for 1 prediction step) when injecting noise to the fuse layer in CVPR18.

C. A new architecture fitted to the content-based saliency

From the above analysis, we can therefore identify some important elements an architecture must feature to better deal with a noisier saliency when extracted from the content, than when provided by the ground-truth users’ statistics. First, if the content-based saliency may still hold relevant (yet noisier) information that may help the prediction in the late prediction steps, then having an LSTM filtering out the noise by canceling the input to the FC layer in the first prediction steps should help. It would let information from the saliency map enter the fusion layers in the late time-steps only. Let us recall there is a difference between time-stamp t and prediction step s , as

defined in Sec. II-A. Second, replacing the FC layers of the fusion module with another LSTM would provide more lever to enable a time-dependent correction of the position-LSTM output with the saliency information.

Making these two modifications, we come up with the architectural block depicted in Fig. 18, that we embed into a seq2seq framework. Interestingly, it is not new and has been proposed by Sadeghian et al. in [36] to predict a pedestrian’s trajectory based on the image of the environment, the past ego trajectory and the trajectories of others. Other architectures aiming at processing and fusing heterogeneous temporal information have indeed been proposed in other application domains. For example, in [37], an architecture akin to NOSSDAV17 has been proposed to decide how to rotate a camera to extract as much information as possible from the least amount of captured FoVs. As we adapt the architectural block proposed in [36] for our dynamic head motion prediction problem, we simply name the resulting architecture **ICCV17** and represent it in Fig. 18. The main features of this deep architecture are 3 LSTM layers, each handling respectively the time series of saliency maps, the time series of positions and the fusion between both intermediate outputs (embeddings). For the same reasons as in Sec. V, we assemble this building block into a seq2seq framework, as shown in Fig. 18. A doubly-stacked LSTM with 256 units each, processes the flattened saliency map pre-generated for each time-stamp. To process the head orientation input, another set of doubly-stacked LSTM with 256 units is used. The multimodal fusion is then handled by a third set of doubly-stacked LSTM with 256 units. Finally a FC layer with 256 and a FC layer with 3 neurons is used to predict the (x,y,z) coordinates, as described in Sec. V.

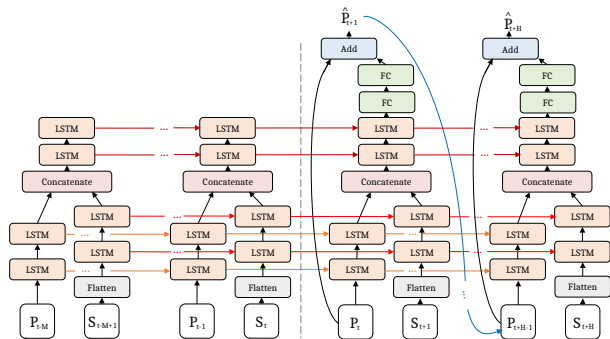


Fig. 18: Seq2seq ICCV17 architecture inspired on [36].

Fig. 16 (magenta line) shows that this architecture is indeed able to significantly outperform CVPR18-improved when fed with the CB saliency. In particular, we observe that ICCV17 is able to get as good results as the position-only baseline in the first time-steps, and significantly improves over the position-only baseline for some videos (in particular the Static focus video Warship) for the late prediction time-steps as shown in Fig. 20.

Also, for the same problem settings (prediction horizons) and datasets as the existing works analyzed in Sec. III-C, we report the results of ICCV17 with the CB saliency in Fig. 5 and Tables II to IV. We confirm that ICCV17 outperforms all

the existing methods, but does not outperform the position-only baseline on these prediction horizons, as discussed in Sec. IV-B.

D. Ablation study of ICCV17

To confirm our hypothesis that led us to introduce this new architecture for dynamic head motion prediction, we lastly run an ablation study of the additional elements we brought compared with CVPR18-improved: as shown in Fig. 19, we either replace the LSTM processing the CB saliency with two FC layers (curve named AblatSal in the legend), or replace the fusion LSTM with two FC layers (curve named AblatFuse).

Fig. 19 and 20 confirm that the removal of the first extra LSTM (compared with CVPR18) processing the saliency input has more impact: the result in the first time-steps degrades (up to the no-motion baseline error). The degradation is not as acute as in CVPR18-improved as the fusion LSTM can still partly filter out the noise, yet it seems that the increased level of noise entering the fusion LSTM makes it cancel most of its input and output a zero motion, as the performance of AblatSal is consistently similar to that of the no-motion baseline. The impact of removing the fusion LSTM is less important, but the curves AblatFuse show that it helps benefit from the saliency information in the late time-steps (while AblatSal shows that the LSTM processing the saliency is crucial not to let the prediction in the first time-steps to degrade away from the position-only baseline).

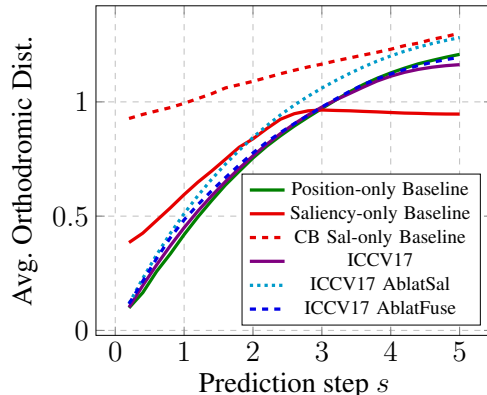


Fig. 19: Results of the ablation of the ICCV17 architecture.

VII. CONCLUSION

In this article we have reviewed and classified existing methods for the dynamic head prediction problem in 360° videos. We have shown the startling result that all these methods perform worse than a trivial no-motion baseline, which can however be outperformed by the position-only baseline we then introduced. To understand the worse performance of the existing methods, we carried out a root cause analysis. We showed that on videos where the content can inform the head position prediction, it can do so for horizons longer than 2 to 3s, the trajectory inertia being predominant earlier. We also showed that a sequence-to-sequence auto-regressive framework is crucial for efficient long-term prediction, and identified

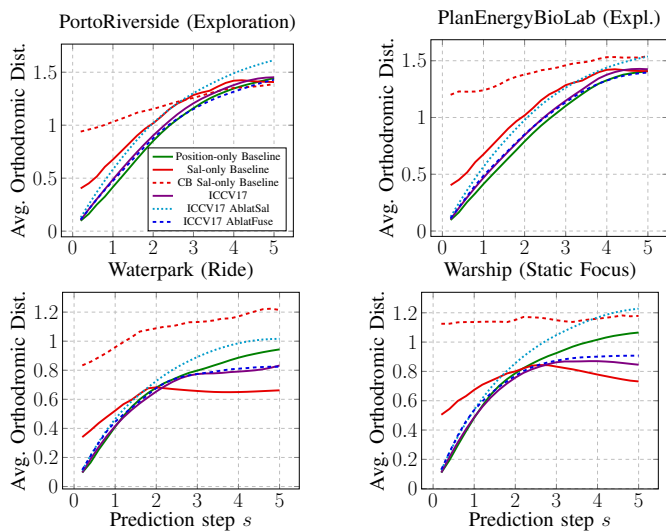


Fig. 20: Per-video results of the ablation study of ICCV17.

that having a dedicated recurrent network to only handle the time series of positions enables to reach the performance of the position-only baseline in the early prediction steps. Finally we showed how the level of noise in the estimated saliency impacts the architecture’s performance, and proposed a new architecture better suited at filtering out the saliency detrimental for the early prediction while letting out relevant information for the later steps.

Two important research directions arise from our findings. First, saliency models must be improved to predict attention in VR, possibly making them time-dependent and fitted to long-term horizons (more than 2s). Sharp contrast seems indeed dominant in PanoSalNet, while a more object-oriented approach seems more in agreement with the salient points. Second, the question of fitting the saliency extraction module to the very prediction task at hand, by training it end-to-end along with the time processing and fusion modules, is worth investigating. We believe this is made easier by our findings on the impact of noise on the different architectural choices.

REFERENCES

- [1] International Data Corporation., “Demand for augmented reality/virtual reality headsets expected to rebound in 2018,” Industry report, 2018.
- [2] J. Park, P. A. Chou, and J.-N. Hwang, “Rate-utility optimized streaming of volumetric media for augmented reality,” *arXiv preprint arXiv:1804.09864*, 2018.
- [3] F. Qian, L. Ji, B. Han, and V. Gopalakrishnan, “Optimizing 360 video delivery over cellular networks,” in *Workshop on All Things Cellular: Operations, Applications and Challenges*. ACM, 2016, pp. 1–6.
- [4] M. Xiao, C. Zhou, V. Swaminathan, Y. Liu, and S. Chen, “BAS-360: Exploring spatial and temporal adaptability in 360-degree videos over HTTP/2.” INFOCOM, 2018.
- [5] H. Hristova, X. Corbillon, G. Simon, V. Swaminathan, and A. Devlic, “Heterogeneous spatial quality for omnidirectional video,” in *IEEE MMSP*, Aug 2018, pp. 1–6.
- [6] A. T. Nasrabadi, A. Mahzari, J. D. Beshay, and R. Prakash, “Adaptive 360-degree video streaming using scalable video coding,” in *ACM Int. Conf. on Multimedia*, 2017, pp. 1689–1697.
- [7] M. Xu, Y. Song, J. Wang, M. Qiao, L. Huo, and Z. Wang, “Predicting head movement in panoramic video: A deep reinforcement learning approach,” *IEEE Trans. on PAMI*, 2018.
- [8] Y. Xu, Y. Dong, J. Wu, Z. Sun, Z. Shi, J. Yu, and S. Gao, “Gaze prediction in dynamic 360° immersive videos,” in *IEEE CVPR*, 2018, pp. 5333–5342.
- [9] A. Nguyen, Z. Yan, and K. Nahrstedt, “Your attention is unique: Detecting 360-degree video saliency in head-mounted display for head movement prediction,” in *ACM Int. Conf. on Multimedia*, 2018, pp. 1190–1198.
- [10] Y. Li, Y. Xu, S. Xie, L. Ma, and J. Sun, “Two-layer fov prediction model for viewport dependent streaming of 360-degree videos,” in *EAI Int. Conf. on Communications and Networking (ChinaCom)*, Chengdu, China, Oct. 2018.
- [11] C.-L. Fan, J. Lee, W.-C. Lo, C.-Y. Huang, K.-T. Chen, and C.-H. Hsu, “Fixation prediction for 360 video streaming in head-mounted virtual reality,” in *ACM NOSSDAV*, 2017, pp. 67–72.
- [12] J. Gutiérrez, E. J. David, A. Coutrot, M. P. Da Silva, and P. Le Callet, “Introducing un salient360! benchmark: A platform for evaluating visual attention models for 360° contents,” in *IEEE Int. Conf. on Quality of Multimedia Exp. (QoMEX)*, 2018.
- [13] Y. Su and K. Grauman, “Making 360 video watchable in 2d: Learning videography for click free viewing,” in *IEEE CVPR*, July 2017, pp. 1368–1376.
- [14] Y. Yu, S. Lee, J. Na, J. Kang, and G. Kim, “A deep ranking model for spatio-temporal highlight detection from a 360 video,” in *AAAI*, 2018.
- [15] M. Zhang, K. T. Ma, J. H. Lim, Q. Zhao, and J. Feng, “Deep future gaze: Gaze anticipation on egocentric videos using adversarial networks,” in *IEEE CVPR*, July 2017, pp. 3539–3548.
- [16] Y. Huang, M. Cai, Z. Li, and Y. Sato, “Predicting gaze in egocentric video by learning task-dependent attention transition,” in *ECCV 2018*, V. Ferrari, M. Hebert, C. Sminchisescu, and Y. Weiss, Eds., 2018, pp. 789–804.
- [17] A. D. Aladaglı, E. Ekmekcioglu, D. Jarnikov, and A. Kondoz, “Predicting head trajectories in 360° virtual reality videos,” in *IEEE Int. Conf. on 3D Immersion (IC3D)*, 2017.
- [18] Y. Ban, L. Xie, Z. Xu, X. Zhang, Z. Guo, and Y. Wang, “Cub360: Exploiting cross-users behaviors for viewport prediction in 360 video adaptive streaming,” in *IEEE Int. Conf. on Multimedia and Expo (ICME)*, 2018.
- [19] I. Sutskever, O. Vinyals, and Q. V. Le, “Sequence to sequence learning with neural networks,” in *Adv. in Neural Info Proc. Sys. (NEURIPS)*, 2014, pp. 3104–3112.
- [20] Supplementary material., “Supplementary material to submission.” 2019.
- [21] J. Martinez, M. J. Black, and J. Romero, “On human motion prediction using recurrent neural networks,” in *IEEE CVPR*, 2017, pp. 4674–4683.
- [22] C. H. Sudre, W. Li, T. Vercauteren, S. Ourselin, and M. J. Cardoso, “Generalised dice overlap as a deep learning loss function for highly unbalanced segmentations,” in *Deep Learning in Medical Image Analysis and Multimodal Learning for Clinical Decision Support*. Springer, 2017, pp. 240–248.
- [23] Y. Li, Y. Xu, S. Xie, L. Ma, and J. Sun, “Two-layer FoV prediction model for viewport dependent streaming of 360-degree videos,” in *Int. Conf. on Comm. and Netw. in China (ChinaCom)*, 2018, pp. 501–509.
- [24] F. Chollet *et al.*, “Keras,” <https://keras.io>, 2015.
- [25] F. Pedregosa, G. Varoquaux, A. Gramfort, V. Michel, B. Thirion, O. Grisel, M. Blondel, P. Prettenhofer, R. Weiss, V. Dubourg, J. Vanderplas, A. Passos, D. Cournapeau, M. Brucher, M. Perrot, and E. Duchesnay, “Scikit-learn: Machine learning in Python,” *Journal of Machine Learning Research*, vol. 12, pp. 2825–2830, 2011.
- [26] D. P. Kingma and J. Ba, “Adam: A method for stochastic optimization,” *arXiv preprint arXiv:1412.6980*, 2014.
- [27] E. J. David, J. Gutiérrez, A. Coutrot, M. P. Da Silva, and P. L. Callet, “A dataset of head and eye movements for 360° videos,” in *ACM MMSys*, 2018, pp. 432–437.
- [28] P. Luc, N. Neverova, C. Couprie, J. Verbeek, and Y. LeCun, “Predicting deeper into the future of semantic segmentation,” in *IEEE ICCV*, 2017.
- [29] A. Alahi, K. Goel, V. Ramanathan, A. Robicquet, L. Fei-Fei, and S. Savarese, “Social LSTM: Human trajectory prediction in crowded spaces,” in *IEEE CVPR*, 2016.
- [30] V. Sitzmann, A. Serrano, A. Pavel, M. Agrawala, D. Gutierrez, B. Masia, and G. Wetzstein, “Saliency in VR: How do people explore virtual environments?” *IEEE Trans. on Viz. and Comp. Graphics*, vol. 24, no. 4, pp. 1633–1642, 2018.
- [31] M. Almquist, V. Almquist, V. Krishnamoorthi, N. Carlsson, and D. Eager, “The prefetch aggressiveness tradeoff in 360 video streaming,” in *ACM MMSys*, 2018.

- [32] J. P. Magliano and J. M. Zacks, "The impact of continuity editing in narrative film on event segmentation," *Cognitive Science*, vol. 35, no. 8, pp. 1489–1517, 2011.
- [33] A. Nguyen, Z. Yan, and K. Nahrstedt, "Panosalnet - source code for Your Attention is Unique: Detecting 360-degree video saliency in head-mounted display for head movement prediction," <https://github.com/phananh1010/PanoSalNet>, 2019.
- [34] K. Simonyan and A. Zisserman, "Very deep convolutional networks for large-scale image recognition," *arXiv preprint arXiv:1409.1556*, 2014.
- [35] X. Huang, C. Shen, X. Boix, and Q. Zhao, "Salicon: Reducing the semantic gap in saliency prediction by adapting deep neural networks," in *IEEE ICCV*, 2015, pp. 262–270.
- [36] A. Sadeghian, A. Alahi, and S. Savarese, "Tracking the untrackable: Learning to track multiple cues with long-term dependencies," in *IEEE ICCV*, 2017, pp. 300–311.
- [37] D. Jayaraman and K. Grauman, "Learning to look around: Intelligently exploring unseen environments for unknown tasks," in *IEEE CVPR*, 2018.